Published online 11 May 2010 *Nucleic Acids Research, 2010, Vol. 38, No. 17* ***5807–5816***
doi:10.1093/nar/gkq344

Cation-dependent cleavage of the duplex form of the subtype-B HIV-1 RNA dimerization initiation site

Eric Ennifar, Philippe Walter and Philippe Dumas*

Architecture et Réactivité de l'ARN, Université de Strasbourg, Institut de Biologie Moléculaire et Cellulaire du CNRS, 15 rue René Descartes F-67084 Strasbourg, France

Received March 9, 2010; Revised April 15, 2010; Accepted April 19, 2010

ABSTRACT

The crystal structure of subtype-B HIV-1 genomic RNA Dimerization Initiation Site duplex revealed chain cleavage at a specific position resulting in 3′-phosphate and 5′-hydroxyl termini. A crystallographic analysis showed that Ba^{2+}, Mn^{2+}, Co^{2+} and Zn^{2+} bind specifically on a guanine base close to the cleaved position. The crystal structures also point to a necessary conformational change to induce an 'in-line' geometry at the cleavage site. In solution, divalent cations increased the rate of cleavage with pH/pKa compensation, indicating that a cation-bound hydroxide anion is responsible for the cleavage. We propose a 'Trojan horse' mechanism, possibly of general interest, wherein a doubly charged cation hosted near the cleavage site as a 'harmless' species is further transformed *in situ* into an 'aggressive' species carrying a hydroxide anion.

INTRODUCTION

All retroviral genomes consist in two homologous single stranded RNAs non-covalently linked near their 5′ ends. Dimerization is an essential step for viral replication. By facilitating template switching of the reverse transcriptase, dimerization increases recombination and, therefore, variability of the viral genome. The Dimerization Initiation Site (DIS) has been identified as a strongly conserved (1) stem-loop structure located in the 5′ non-coding leader region of the genomic RNA (2,3) (Figure 1). However, some variations of the nine-nucleotide DIS loop sequence are tolerated, depending on HIV-1 isolates: $A_{272}G\underline{GUGCAC}A_{280}$ is mainly found in HIV-1 subtypes A and G, $A_{272}A\underline{GCGCGC}A_{280}$ in subtypes B and D, $A_{272}A\underline{GCGCGC}U_{280}$ in subtype C and $A_{272}A\underline{GUGCAC}A_{280}$ in subtypes F and H. The loop contains a 6-nt self-complementary sequence (underlined) which initiates dimerization by forming a loop-loop complex, or 'kissing-complex' (Figure 1). The stability of this complex is strongly dependent on the three flanking nucleotides (mainly purines) surrounding the self-complementary sequence (4,5). It was shown *in vivo* that alteration of the DIS sequence strongly affects RNA dimerization, packaging and dramatically reduces viral infectivity (6–9). *In vitro* assays have shown that the kissing-loop complex can be converted into a more stable extended duplex upon incubation at 55°C, or by the nucleocapsid protein at 37°C (10–14) (Figure 1). It has also been shown that kissing-loops formed by the 23-mer DIS RNA used in this study (Figure 1) can be spontaneously converted into duplex at 37°C (13,15–17). Such a conversion observed *in vitro* with short RNA fragments is invariably presented as accounting for the stabilization of genomic RNA dimers observed during maturation of viral particles (18). Such an explanation is certainly appealing and plausible but, as far as we know, a formal proof of the occurrence *in vivo* of this often mentioned mechanism is still lacking.

We have previously solved crystal structures of the HIV-1 subtype-A and -F DIS duplex (19,20), and of subtype-A, -B and -F DIS kissing-complex (21,22). These structures revealed unexpected and astonishing structural and sequence similarities between the DIS dimer and the bacterial 16 S ribosomal RNA aminoacyl decoding site (A site). Owing to this resemblance, we have shown that the DIS tightly bind aminoglycoside antibiotics (17,20,23,24). This finding opens interesting structure-based drug design perspectives for targeting specifically the HIV-1 DIS with aminoglycoside-based molecules (25,26).

Here, we report the 1.6 Å resolution crystal structure of the subtype-B DIS extended duplex form. The structure shows some differences compared with HIV-1 subtype-A and -F duplexes (Supplementary Figure S1). The most striking feature is a clear cut in the electron density between G_{271} and A_{272} showing 5′-hydroxyl and 3′-phosphate termini. The cleavage was also observed in solution and shown to require divalent cations with a strong dependence on their ability to downshift the pKa of coordinated water molecules.

*To whom correspondence should be addressed. Tel: +33 388 41 70 02; Fax: +33 388 60 22 18; Email: p.dumas@ibmc.u-strasbg.fr

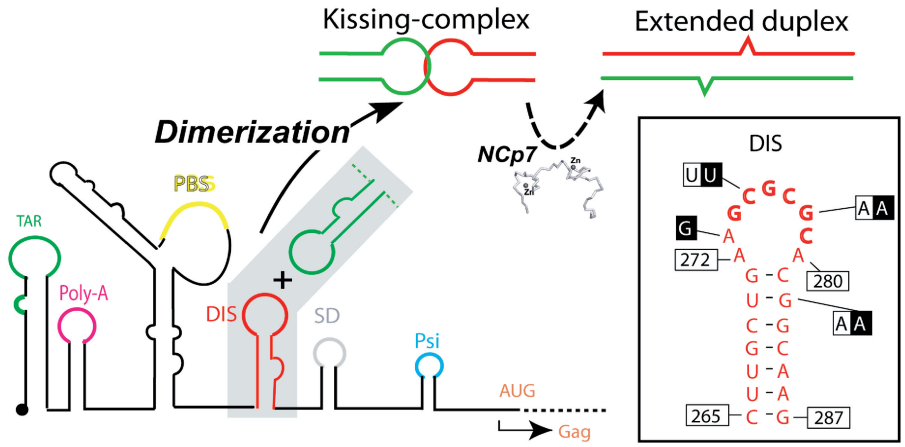

Figure 1. Location and mechanism of HIV-1 RNA dimerization. Schematic drawing of the HIV-1 RNA dimerization mechanism, involving the DIS of two homologous strands (in red and green). The insert shows the subtype-B HIV-1 23-nt DIS fragment used in this study. Changes corresponding to the subtype-A and –F HIV-1 DIS sequence are represented in black and white boxes, respectively.

MATERIALS AND METHODS

RNA synthesis, purification and crystallization

The 23-mer chemically synthesized subtype-B DIS RNA was purchased from Dharmacon and purified using an ion-exchange Nucleopac PA-100 column as described (27). RNA at a concentration of 60 µM was annealed for 3 min in water at 90°C and cooled to room temperature. It was then incubated for 1 h at 37°C in a crystallization buffer (20 mM Na cacodylate pH 7.0, 5 mM $MgCl_2$, 300 mM KCl) and concentrated to 500–600 µM. Crystallization was performed in sitting drop by adding one volume of crystallization solution made with MPD (20%) and spermine (50 mM) to nine volumes of RNA in the crystallization buffer. Drops were equilibrated at 37°C with a reservoir made with 50% MPD, 50 mM Na cacodylate, 100 mM $MgCl_2$ and 300 mM KCl. Platelets crystals appeared within 4–10 days and were stabilized at 20°C and cryo-protected by soaking in reservoir solution.

Crystal soaking, X-ray data collection and processing

Heavy atom derivatives for the MIR method were obtained by soaking crystals for several days in a reservoir solution containing 25 mM ruthenium(III) hexamine (without magnesium) or 10 mM $AuCl_3$ (in presence of 100 mM $MgCl_2$). Soaking of crystals was also performed for the determination of the binding sites of cations inducing cleavage. Daylong soaking of the crystals in 100 mM Mn^{2+} or Ba^{2+} was possible without affecting their diffraction power; for zinc and cobalt, it was necessary to reduce salt concentration to 20 mM and the soaking time to ~1 h. After stabilization, crystals were flash-cooled in liquid ethane (simple flash cooling under the nitrogen gas stream usually resulted in a serious loss of diffraction). All data were collected at 100 K (Tables 1 and 2), and processed using the HKL package (28).

Structure solution and refinement of structures

Two strong heavy atom sites were localized using anomalous differences with LOCHVAT (29,30) for the gold derivative. Subsequently, three ruthenium-binding sites were localized by Fourier-difference maps. Phasing was initiated at 2.0 Å resolution with SHARP 3.0 (31) using the gold derivative, and not the native, as the reference dataset. The figure of merit was greatly improved by solvent flattening with SOLOMON (32) using a solvent content of 40%. The resulting experimental map was of excellent quality, revealing one dimer per asymmetric unit

Table 1. Data collection summary and phasing statistics for structure solution

	Native	$Ru^{3+}(NH_3)_6$	Au^{3+}
X-ray source	ESRF ID14-2	ESRF BM30	ESRF BM30
Wavelength (Å)	0.93	0.92	0.92
Max. Resolution (Å)	1.60	1.98	2.30
Completeness[a] (%)	99.5 (99.0)	98.9 (99.3)	99.7 (99.9)
Redundancy	9.2	11.2	6.8
Mean I/σ[a]	23.8 (10.0)	53.2 (15.4)	37.0 (10.4)
R_{sym}[a] (%)	6.3 (24.0)	6.9 (13.5)	4.2 (10.4)
Phasing power[b]			
centric	1.0	0.87	–
acentric (iso/ano)	1.0/–	1.0/–	–/2.5
R_{cullis}[c] (centric)	0.89	0.84	–

Space group: $P2_12_12$; unit cell a = 44.0 Å, b = 47.5 Å, c = 57.7 Å. Mean figure of merit before/after solvent flattening: 0.38 (0.07)/0.86 (0.80).
[a]Values in parenthesis are those for outermost shell.
[b]Phasing power = $<F_H/LOC>$, where LOC is the lack of closure.
[c]$R_{cullis} = \| |F_{PH} \pm F_P| - F_H| / |F_{PH} - F_P|$ for centric reflections.

Table 2. Data collection summary for divalent metal-soaked structures

	Mn^{2+}	Zn^{2+}	Co^{2+}	Ba^{2+}
X-ray source	ESRF BM30	ESRF BM30	Rot. anode	Rot. anode
Wavelength (Å)	1.41	1.28	1.54	1.54
Max. Resolution (Å)	2.60	1.90	2.35	2.56
Completeness (%)	98.4 (92.7)	87.0 (41.9)	94.2 (94.6)	99.2 (94.5)
Redundancy	3.3	4.8	2.4	5.6
Mean I/σ	21.1 (12.0)	19.7 (10.1)	14.1 (2.2)	27.5 (12.4)
R_{sym} (%)	6.0 (8.3)	6.8 (8.5)	6.1 (38.2)	6.5 (13.2)

Values in parentheses are those for outermost shell.

packed along the c axis so as to form pseudo-infinite helices. The model was built with O 6.2 (33) and structures of pre-cleaved and post-cleaved were refined with CNS (34) (Table 3). Potassium, zinc, cobalt and manganese ions were identified using anomalous Fourier-difference maps as described (19).

Analysis of RNA cleavage in solution

The 23-mer DIS RNA at a concentration of 90 μM in water was heated at 90°C for 5 min. and slowly cooled to room temperature for several hours to allow duplex formation. The sample was then diluted to 12 μM in a buffer containing 150 mM potassium acetate, 20 mM sodium cacodylate pH 6.85 or pH 6.31, and 5 or 20 mM of divalent cations ($MgCl_2$, $MnCl_2$, $ZnCl_2$, $CoCl_2$, $BaCl_2$, Pb(II) acetate) or 3 mM EDTA, and incubated at 37°C. Lead acetate was used for its higher solubility in comparison of lead chloride. Slightly acidic conditions prevented the formation of insoluble hydroxides. For visualization of the 5′-cleavage product and quantification, 5′[γ^{32}P]ATP-labelled RNA was mixed with unlabelled RNA. The RNA was analysed on denaturing 8 M urea, 20% polyacrylamide gel electrophoresis (DPAGE) in TBE buffer (45 mM tris–borate pH 8.3, 2 mM EDTA) and the cleavage position was checked using RNase T1 and alkaline ladders. Gel quantification was made with a Fuji phosphoimager. Raw data from the phosphoimager software were obtained as binary image files. To transform the raw value at each pixel of the image into a value proportional to the radioactivity count, the following transformation $\text{RawValue} \rightarrow 10^{4\times\text{RawValue}}$ (unimportant pre-exponential factors are omitted) was initially applied, according to information from the manufacturer. We found it necessary to refine the latter transformation as $\text{RawValue} \rightarrow 10^{3.86\times\text{RawValue}}$ to fit correctly the response obtained from a known dilution scale. When the cleavage was fast enough, as for Pb^{2+}, the cleavage rate constants k could have been derived following the relation $f_{obs} = 1 - e^{-kt}$ where f_{obs} is the fraction of cleaved RNA (Supplementary Figure S13b). However, in situations of slow and incomplete cleavage, as for Co^{2+}, Mn^{2+} or Mg^{2+}, the inescapable variations in the amount of radioactive materials loaded in each lane of the gel made this procedure too inaccurate. An internal standardization was thus used within each lane by considering also the small-size products (Supplementary Figures S10 and S13a). The procedure is explained in Supplementary Data. The fact that the results show a very similar pattern at the two pH values (Figure 5b) may be viewed as an indication that the procedure was effective. All calculations, comprising image gel processing, were made with *Mathematica* from Wolfram Research.

Table 3. Refinement statistics

	Native	Mn^{2+} soaked	Co^{2+} soaked
Max. resolution (Å)	1.6	2.6	2.4
Completeness (work + test sets)	95.4%	97.7%	91.2%
R_{free} factor	25.0%	23.0%	28.4%
R factor	24.2%	20.0%	23.9%
Estimated coordinate errors (Å)	0.22	0.34	0.36
Average B factor (Å^2)	32.0	20.4	42.0
Number of nucleic acid atoms	982	982	982
Number of water molecules	183	149	46
Number of metal atoms	5	8	5
Protein Data Bank ID	2OIY	2OJ0	3FAR

RESULTS

Description of the structure

As observed in previously described crystal structures of DIS extended duplex, the subtype-B DIS extended duplex structure looks quite similar to its kissing-complex counterpart (21,22) in spite of the different RNA topology (Supplementary Figure S2). The structure is mainly characterized by A_{272} and A_{273} of both strands related by non-crystallographic symmetry (named strands a and b in the following) being extrahelical and forming a four-base stack, the A_{280} of each strand remaining unpaired inside the helix (Figure 2). A comparison of these flanking purines among various DIS crystal structures are described in Supplementary Data (Supplementary Figure S3). In spite of a local phosphate backbone distortion induced by the inter-strand adenine stacking, the duplex remains perfectly linear (Figure 2b). In the present structure, A_{273a} and A_{273b} are involved in 'A-minor' (35,36) contacts with the minor groove of a symmetry-related duplex molecule, leading to an interaction very similar to one described in the 30 S ribosomal subunit [see Figure 7b in (37)]. It may be hypothesized that such an interaction occurs within the complete

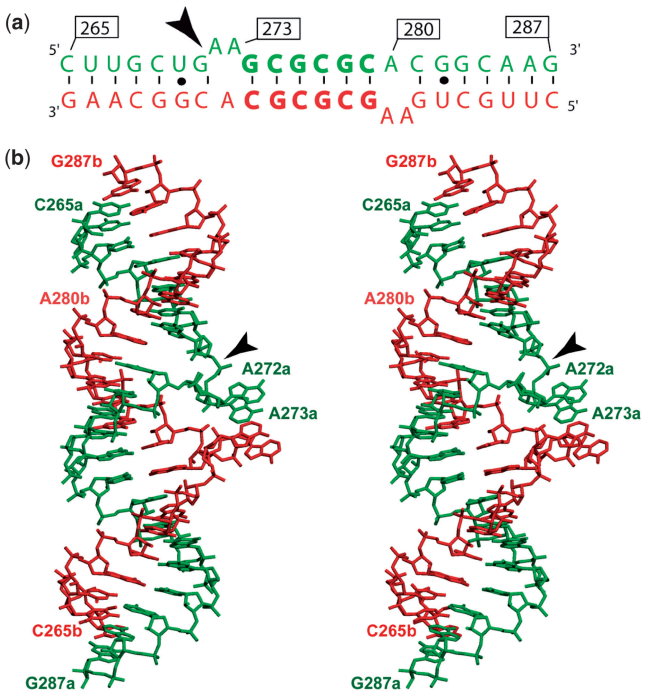

Figure 2. Structure of the HIV-1 subtype-B DIS extended duplex. The two strands are represented in green and red. The black arrowhead depicts the asymmetric cleavage site observed in crystals. (**a**) Sequence and secondary structure of the duplex. (**b**) Stereo view of the structure solved in this study.

encapsidation region in the viral RNA after dimerization and maturation of virions (38,39).

The subtype-B DIS duplex is cleaved in crystals and in solution

The most striking feature of the subtype-B duplex structure is the presence of a cleavage between G_{271} and A_{272} of one of the two strands (strand a in green on Figure 2b). The cleavage was first revealed during refinement of the structure by inspection of electron density maps from several crystals. It appeared on (Fo–Fc) difference Fourier maps as a strong positive peak close to ribose 271a, which corresponds to the position of the phosphate after cleavage, and as a strong negative peak on its expected position before cleavage (Figure 3a). In agreement with this interpretation, a composite simulated annealing omit map showed a very poor density for the ribose of G_{271a} in a C2′-*endo* conformation, and for the G_{271a}-A_{272a} phosphodiester bond. The cleavage was confirmed by a polyacrylamide gel analysis of RNA from dissolved crystals and from drops where they had grown (Figure 3b). Furthermore, inspection of various electron density maps clearly showed an alternative C3′-*endo* conformation of the G_{271a} ribose and a 3′-phosphate resulting from cleavage. This suggested that cleavage proceeds through the classical mechanism of nucleolytic ribozymes by a two-step reaction involving first a trans-esterification producing strand scission and a 2′-3′-cyclic phosphate intermediate and, second, followed by its hydrolysis resulting in the 3′-phosphate product [Supplementary Figure S4; for review, see (40)]. Such a mechanism was first observed for the tRNA(Phe) (41,42), and for lead-dependent ribozymes (43), but not with hammerhead, hairpin and hepatitis δ ribozymes that are unable to catalyse hydrolysis of the 2′-3′-cyclic phosphate produced by the first trans-esterification [for review, see (44,45)].

Surprisingly, whereas one strand in the crystals was cleaved to within 30–40% (which was estimated by refining the occupancy of the pre- and post-cleaved conformations of G_{271a}), no significant cleavage could be detected at G_{271b} on the other strand related by non-crystallographic symmetry. In agreement with this observation the ribose of G_{271b} clearly appeared in the C2′-*endo* conformation as predominantly observed in absence of cleavage at that stem terminal base-pair (21,22). Altogether, these observations are strongly in favour of the existence of cation-dependent cleavage in the crystals. This obviously does not exclude that a part of the RNA molecules integrated in a crystal were previously cleaved in solution.

Crystallographic study of cation binding near the cleavage site

To understand the role of metal ions in the primary cleavage mechanism, we soaked crystals for several days with magnesium-free solutions containing either manganese, zinc, barium or cobalt divalent cations. Anomalous difference maps for manganese, zinc and cobalt (for barium, see below) revealed a strong peak in the vicinity of G_{271a} for manganese [11.5 estimated standard deviations (e.s.d.)], zinc (19.5 e.s.d.) and cobalt (8.9 e.s.d.) (Figure 4a and Supplementary Figures S5 and S6). In addition, simulated annealing composite omit maps showed a conformational change of the sugar–phosphate backbone between residues 273a and 274a, resulting in an inward rotation of phosphate 274a and an outward 2.3 Å translation movement of G_{274a} (Figure 4b). This local conformational change creates a negatively charged metal ion pocket, where the partially dehydrated divalent ion is directly bound to N7 of G_{274a}, and to anionic oxygen atoms of phosphates 273a and 274a (Figure 4a). This contrasts with the catalytic divalent cation bound by outer-sphere coordination to the active site of the HDV ribozyme (46). Notably, the residues surrounding G_{274a}, including the bulged adenines, are not affected by this motion, and the base pair G_{274a}-C_{279b} is not disrupted (Figure 4a). Although the cation binding scheme is similar for Mn^{2+} and Zn^{2+}, the distance from each cation to the 2′-OH group of the cleaved G_{271a} residue

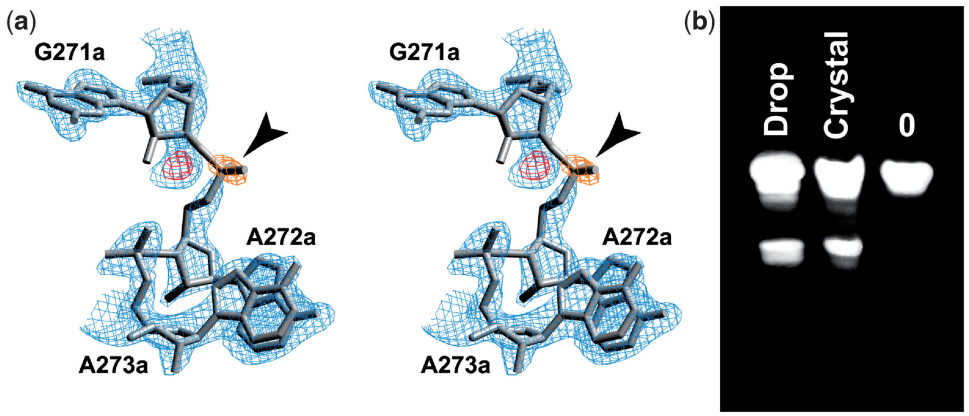

Figure 3. Cleavage observed in the HIV-1 subtype-B extended duplex. (**a**) Stereo view of the cleaved region. The model used for electron density map calculations corresponds to the uncleaved form. (3Fo–2Fc) electron density map contoured at 1.4 e.s.d. is shown in blue; (Fo–Fc) difference map is shown contoured at 5.0 e.s.d. (red), and –3.5 e.s.d. (orange). The latter shows an excess of density on phosphate 272 as built in the uncleaved model (negative peak), and a lack of density (positive peak) corresponding to its position after the cleavage. (**b**) Denaturing PAGE analysis of RNA extracted from crystallization drop, from a dissolved crystal, and before crystallization (0). Only the largest 5′-fragment resulting from cleavage is visible upon ethidium bromide staining.

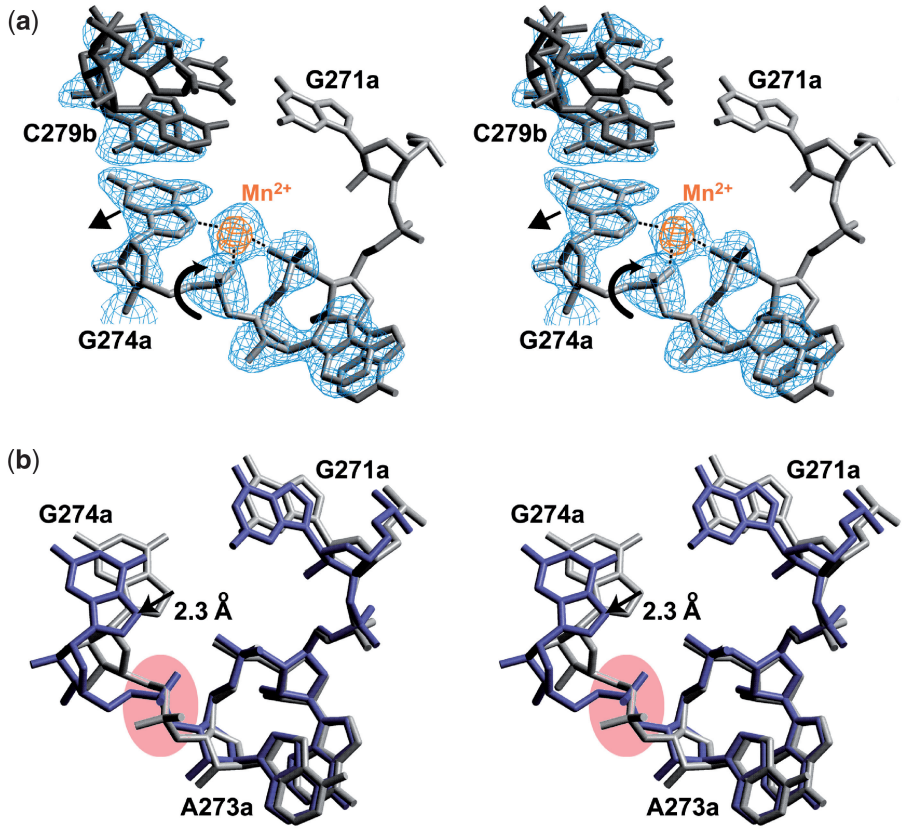

Figure 4. Cation-induced conformational change at the A_{273}–G_{274} step. (**a**) Stereo view of the composite simulated annealing omit map contoured at 1.4 e.s.d. showing a clear density for residues A_{273a} and G_{274a} after the conformation change (indicated with black arrows), without disrupting the G_{274a}–C_{281b} base-pair. The anomalous-difference map corresponding to the manganese ion is represented in orange and contoured at 8.0 e.s.d. The cation lies at 2.4 Å from the N7(G_{274a}) and at 2.3 Å and 2.0 Å from each phosphate. (**b**) Superimposition of the native (in gray) and the manganese-soaked structures (in blue). The binding of Mn^{2+}, Co^{2+} or Zn^{2+} induces a 2.3 Å movement of base and ribose 274, as well as a rotation of phosphate 273 toward the interior of the helix (pink circled region).

varies from 6.5 Å for Mn^{2+} to 5.6 Å for Zn^{2+}. For the latter cation, the anomalous difference map displays a major peak and also, well above the background, an elongated extension which may be the mark of a more complex binding mode (Supplementary Figure S5). Interestingly, no significant peak was detected in anomalous difference map for Zn^{2+} and Mn^{2+} on G_{274b} on the other strand and, concomitantly, the electron density map did not reveal any cleavage at G_{271b}.

For Co^{2+}, on the contrary, a strong peak (7.4 e.s.d.) was also found in an anomalous difference map on G_{274b} and, concomitantly, a cleavage at G_{271b} was observed (Supplementary Figure S6). This confirms that cleavage can take place in the crystals and that divalent cations are involved in the cleavage. The binding mode of Co^{2+} also differs from Zn^{2+} and Mn^{2+} because, first, no inward movement of phosphate 274 is observed, which results in a direct coordination of the cation only to N7 of G_{274} and, second, because the distances between Co^{2+} and 2′-OH groups of G_{274a} and G_{274b} (4.8 and 3.8 Å) are shorter than for their Zn^{2+} counterparts (Supplementary Figure S6). It is difficult to decide whether these differences are related to the different nature of each cation, to enhanced cleavage in the crystal, or to both.

Two strong peaks in an anomalous difference map (13.2 and 11.5 e.s.d.) were also seen with Ba^{2+} on G_{274a} and G_{274b} (Supplementary Figure S7). At variance with other cations, Ba^{2+} is shifted toward O6 of G_{274a} and G_{274b}, which prevents it from a direct coordination with phosphates 273 and 274. Also, no cleavage was visible with Ba^{2+} at G_{271b} and some cleavage was visible at G_{271a}, but very likely this cleavage was due to the presence of Mg^{2+} prior to soaking with Ba^{2+}. Such a peculiarity will be rationalized fully in the following. Finally, this cation binding study also showed, as previously reported (27), that metal ion binding to RNA can be very sensitive to small structural variations since only Ba^{2+} and Co^{2+} were able to bind at the two *a priori* equivalent sites G_{274a} and G_{274b}. Such a non-symmetric binding for Mn^{2+} and Zn^{2+} is likely limited to the crystalline state and, therefore, both strands should be susceptible to cleavage in solution.

Solution study of the cleavage

Although the involvement of the G_{271} 2′-OH group in the cleavage reaction was extremely probable, we confirmed it by using a mutated DIS sequence where this residue was replaced by a deoxyguanosine; as expected, cleaving

activity was abolished (Supplementary Figure S8). We then compared the ability of Mg^{2+}, Mn^{2+}, Zn^{2+}, Co^{2+}, Pb^{2+}, Ba^{2+} and Ca^{2+} to induce strand cleavage in solution. Experiments were performed at 37°C and resulting fragments were separated by denaturing PAGE. Ethidium bromide staining revealed the 16-mer fragment corresponding to the 3′ cleavage product. This also revealed a distinct band, which was unexpected since only one cleavage site could be seen in the crystal structure (Figure 5a). We note that this additional band was absent with Co^{2+}. Essentially, this was the mark of an additional cleavage site at A280, opposite to the cation binding site. More details about this are in Supplementary Data. In the following, the cleavage at G271 and at A280 will be referred to, respectively, as the primary and the secondary cleavage cleavage site.

Under conditions close to those used for crystallization (20 mM Mg^{2+}), the primary cleavage is rather slow compared to small RNA ribozymes. Only 7% of the RNA was cleaved after 14 h of incubation (Figure 5), which yields a rate constant $k_{Mg^{2+}} = 8.6 \times 10^{-5}\,min^{-1}$. In presence of either 3 mM EDTA and 100 mM Na^{+}, or of saturating concentration of cobalt(III) hexammine, no cleavage was detectable even on daylong time-scale, confirming that divalent metal ions are required for the reaction (Supplementary Figure S9 and not shown). We have thus compared the efficiency of cleavage with different cations: Ca^{2+}, Ba^{2+}, Mn^{2+}, Co^{2+}, Zn^{2+} and Pb^{2+} (Figure 5 and Supplementary Figures S9, S10 and S11). Cleavage rates observed for the DIS duplex are comparable to those observed for the secondary cleavage sites in the minimal hammerhead ribozyme (47,48). In our case, the most efficient cation is Pb^{2+}, which led to 42% of cleavage after 1 h at 5 mM concentration ($k_{Pb^{2+}} = \sim 10^{-2}\,min^{-1}$), and the less efficient are Ca^{2+} and Ba^{2+}, which did not promote any detectable cleavage after 14 h (Figure 5a and data not shown).

Analysis of the cleavage rates showed that the ranking of the tested cations for their ability to cleave the duplex correlates very well with their shifting of the pKa of coordinated water molecules since we obtained $\Delta \log k/\Delta pKa = -1.06 \pm 0.1$ at pH 6.30 and $\Delta \log k/\Delta pKa = -0.93 \pm 0.14$ at pH 6.85, where k is the cleavage rate constant (Figure 5b). Therefore, $\Delta \log k/\Delta pKa = -1$ within experimental errors. We also observed that lowering the pH by 0.55 unit (from 6.85 to 6.3) resulted in less cleavage for all cations with a mean value $\langle \Delta \log k/\Delta pH \rangle = 0.98 \pm 0.16$ (Figure 5b). Thus, within experimental errors, there exists a pKa/pH compensation on the kinetics of cleavage, which implies that a cation coordinated to a hydroxide ion is responsible for the activation of the 2′-OH group of G_{271a} leading to cleavage. Indeed, considering the acid-base equilibrium between the two species $M^{2+}(H_2O)_n$ and $M^{2+}(H_2O)_{n-1}OH^{-}$ yields $m = m_0 10^{pH-pK_a}/(1+10^{pH-pK_a})$, where m is the concentration of the cation bearing a hydroxide anion and m_0 is the total cation concentration. This accounts well for the observed pKa/pH compensation.

If the active cationic species were not to be bound to the RNA at some stage prior cleavage, one would expect that, at a given pH, the rate of cleavage should be proportional to the total cation concentration m_0. However, with manganese, for which accurate data could be obtained at both pH, a 4-fold increase of total concentration from 5 to 20 mM yielded $k(20\,mM)/k(5\,mM) = 2.2 \pm 0.15$ at pH 6.85 and $k(20\,mM)/k(5\,mM) = 2.4 \pm 0.5$ at pH 6.30, which are values significantly different from 4. Such a value close to 2.3 agrees well with the need of cation binding to the RNA before cleavage if the binding of Mn^{2+} at 20 mM is in excess to its binding at 5 mM precisely by a factor 2.3. For this to take place the dissociation constant of Mn^{2+} has to be $K_d = \sim 9$ mM. Interestingly, a much more detailed analysis of the same kind was performed for the binding of magnesium to the HDV ribozyme and led to quite comparable values ($K_d = \sim 3.1$ mM at pH 6.5) (49). Furthermore, our value $K_d = \sim 9$ mM fits also well with apparent dissociation constants of various divalent cations (from 5 to 12 mM) that

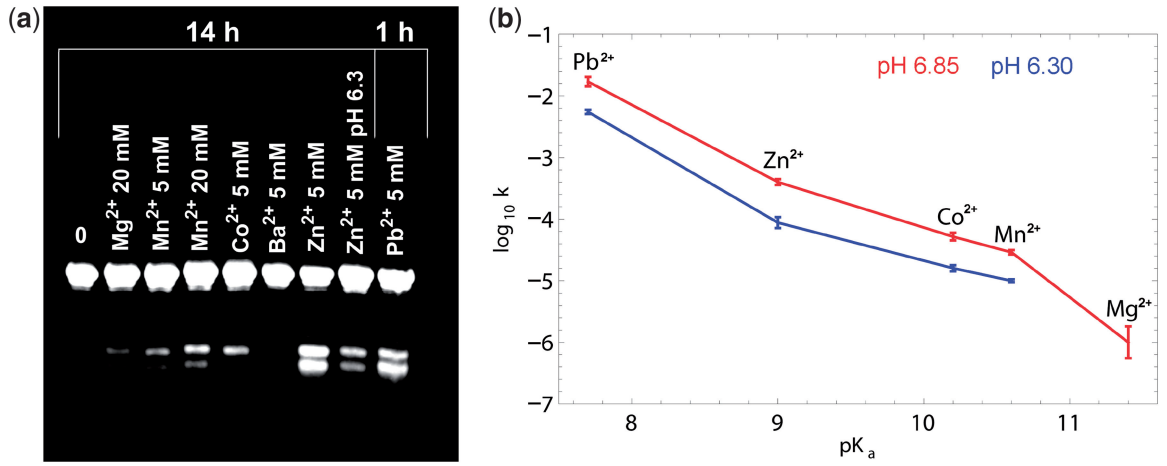

Figure 5. Analysis of the cleavage of 23-mer subtype-B DIS duplex in solution. (**a**) Metal ion dependency of the cleavage at pH 6.85 and 37°C. The cleavage with Zn^{2+} was also performed at pH 6.3. (**b**) Variation at two pH values of the cleavage rate versus the pKa of each cation at 5 mM. The kinetic constant could not be determined at the lower pH for Mg^{2+}. The error bars are those from the numeric procedure exposed in Supplementary Data and are not fully representative of the overall errors which are certainly more important (see text).

were reported for a modified *Schitosoma* hammerhead ribozyme (50). Finally, we also performed competition experiments with Ba^{2+} and Ca^{2+} that are inefficient at cleaving the RNA. As expected, Ba^{2+} as well as Ca^{2+} inhibited the Co^{2+}-dependent cleavage (Supplementary Figure S12). This is consistent with Co^{2+} being dislodged from the specific binding sites by competitive inhibitors (albeit we have a formal crystallographic proof of specific binding only for Ba^{2+}; see Supplementary Figure S7). Half inhibition by Ba^{2+} was seen to take place roughly in the range 6–30 mM (Supplementary Figure S12). Calculation of the inhibition factor shows that this is explained if the K_d of Ba^{2+} is comprised between 5 and 25 mM, which seems also reasonable in view of the values just mentioned. Although competitive inhibition agrees with our results, one cannot exclude that, at the highest Ba^{2+} or Ca^{2+} concentrations, electrostatic screening too (51), and not only direct competition for the crucial binding sites, was responsible for cleavage inhibition.

DISCUSSION

Proposition of a detailed cleavage mechanism

By using the different views of the cleavage site provided by our crystal structures, as well as the results from solution studies, we can propose the following cleavage mechanism for the DIS duplex (Supplementary Figure S4). Clearly, the rather slow cleaving rate observed in this structure compared to 'standard ribozymes' is an advantage for crystallographic studies by allowing the trapping of intermediate states. First, a snapshot of the structure before cleavage is provided by the uncleaved strand, which shows ribose 271 in a C2′-*endo* conformation (Figure 6a). Second, there would be a necessary intermediate consisting in the binding of a divalent cation with a suitable pKa at the A_{273}–G_{274} step; depending on the cation, there is a local rearrangement leading to the involvement of A_{273}, G_{274} phosphates in the binding (Figure 6b). The metal ion would then be able to provide a hydroxide anion accepting a proton from the 2′-OH group of G_{271}. Third, the cleavage reaction would require a crankshaft motion of the A_{272} phosphate towards the interior of the helix to obtain a configuration of the A_{272} scissile bond in line with the O2′ of G_{271} in a C2′-*endo* conformation. A model of such a conformation is shown in Figure 6c. This unstable phosphate conformation, very likely the chemical limiting step, was not observed in our crystal structure, but would be very similar to the one observed at the cleavage site of the fully active extended hammerhead ribozyme (52). Such an in-line conformation was also observed at a secondary cleavage site of the minimal hammerhead ribozyme where it was stabilized by a direct interaction with a zinc cation (48) (Supplementary Figure S13). Such a 2′-OH-mediated nucleophilic attack can only result in strand scission with a 2′-3′-cyclic phosphate and 5′-OH termini. Since the 2′-3′-cyclic phosphate could not be detected in the electron density map, this means that it should be hydrolyzed quickly enough to yield the observed

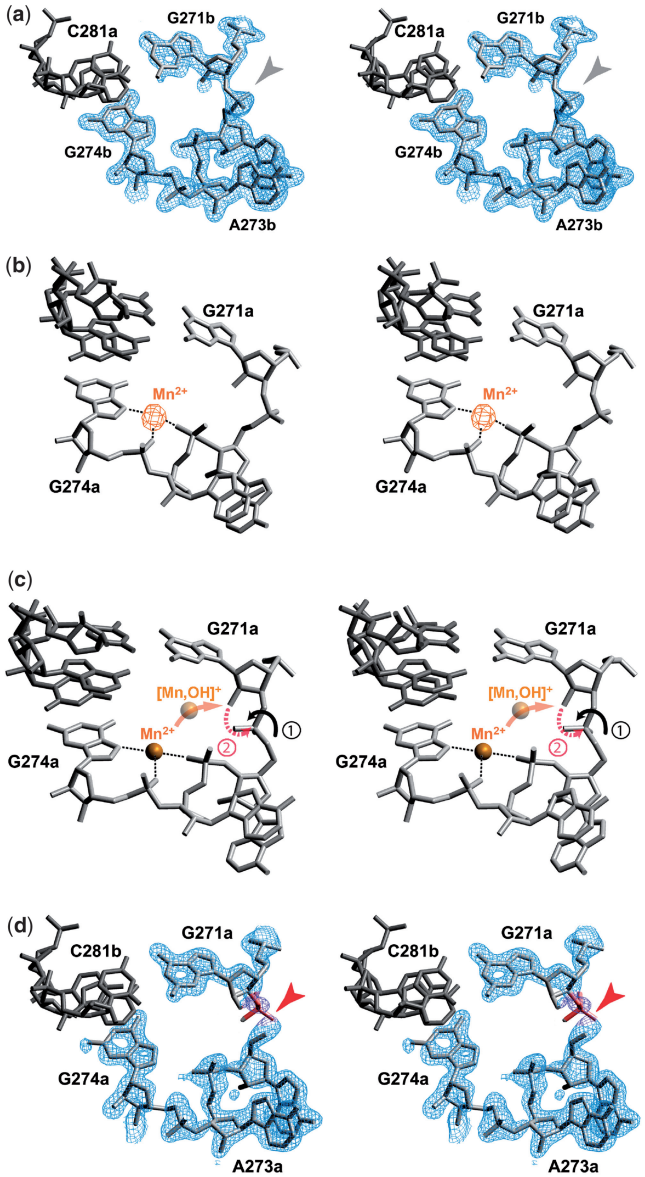

Figure 6. Proposition for a cleavage mechanism. (**a**) Snapshot of the initial state provided by the uncleaved strand. Residue G_{271} is in a C2′-*endo* conformation and no metal ion is present in the pocket, which is closed by an unusual CH8(G_{274})-phosphate(A_{273}) hydrogen bond. The (3Fo–2Fc) electron density map contoured at 1.4 e.s.d. is shown in blue. The gray arrowhead shows the cleavable phosphodiester bond. (**b**) A divalent metal ion (here Mn^{2+}) binds at the A_{273}–G_{274} step, inducing a rearrangement of the sugar-phosphate backbone. The anomalous-difference map contoured at 8.0 e.s.d. is shown in orange. (**c**) The metal ion reduces the pKa of a bound water molecule and generates hydroxide anions that activate the 2′-OH group of the G_{271} ribose. A necessary movement of the phosphate 272 toward the interior of the helix (curved arrow #1) then orients the cleavable bond in-line with the activated 2′-hydroxyl group thus allowing (curved arrow #2) a nucleophilic attack leading to a 2′-3′-cyclic phosphate intermediate. This product is not stable in crystals and is hydrolyzed (**d**) into a 3′-monophosphate (in red) product observed in this simulated annealing composite omit map (contoured at 1.4 e.s.d.).

3′-phosphate product as previously observed with the leadzyme (43). In the absence of a cyclic phosphate the G_{271} ribose is no more constrained and is free to switch from its initial C2′-*endo* to a C3′-*endo* conformation recognizable in electron density maps (Figure 6d).

Clearly, one conflicting observation should be addressed. Indeed, there is a difference between Mg^{2+}, which was not visible in the electron density map and yet is able to cleave (since the original observation of cleavage was in a Mg^{2+}-containing crystal), and other cleaving cations that were visible in electron density maps. This is not unprecedented since the catalytic Pb^{2+} in the leadzyme ribozyme for example (53) could not be localized in crystal structures. In the present case, we have no clear-cut explanation for this difference between Mg^{2+} and other cations. Nevertheless, it may be mentioned that Mg^{2+} (10 electrons) is inherently more difficult to observe than the other cations we used (from 23 to 80 electrons). Furthermore, magnesium has an exceedingly small anomalous scattering component, which makes useless an anomalous difference map to reveal its presence in a specific binding site, if any. Finally, Mg^{2+} might also bind less strongly than Mn^{2+}, Co^{2+} and Zn^{2+}, but sufficiently to provoke cleavage, and/or Mg^{2+} is released after cleavage more easily than Mn^{2+}, Co^{2+} and Zn^{2+}. Either possibility is consistent with the stronger affinity for N7 atom of the latter cations that are softer than Mg^{2+} [in this respect, see (54)].

It is interesting to compare the cleavage pattern observed in the DIS RNA after cation binding at a specific site with an artificial system using lanthanide complexes covalently linked to an oligoDNA hybridized to an oligoRNA (55). When a perfect helical duplex was formed, due to full complementarity of the RNA and DNA sequences, a cleavage was observed, but only at the phosphodiester bond opposite to the nucleotide bearing the lanthanide complex. Interestingly, the position opposite to the cation binding site in the DIS is A280 (Figure 2), where a secondary cleavage was also observed (Supplementary Figures S10 and S11). When the artificial system was designed with an imperfect sequence complementarity allowing an RNA bulge to form in the vicinity of the lanthanide complex, up to four additional consecutive cuts were observed in the stretch of unpaired residues forming the bulge. Overall, the latter observation is strikingly similar to what we observed with the DIS, the primary cleavage site being at G271 next to the extrahelical purines A272, A273 corresponding to the bulged-out residues in the artificial system. However, in our case, a more specific pattern was seen with cobalt which produced no significant cleavage at A280 (opposite to the cation binding site) and almost no additional cleavage surrounding the major cleavage site at G271 (Supplementary Figure S11). This is certainly related, albeit not in an obvious way, to the previously mentioned different binding mode of cobalt versus zinc and manganese. Therefore, what this comparison shows is that the gross features of the cleavage pattern in the DIS do not seem to derive from the genuine specificity of binding of divalent cations, but rather from the cation binding site being close to the covalent bond susceptible to cleavage (see the 'Conclusion' section). Some peculiarities, however, do result from the specificity of binding, as seen with cobalt.

A Trojan horse mechanism?

Since cation binding is a prerequisite for cleavage and since the active species corresponds to a partially neutralized cation carrying a hydroxide anion, a doubly charged cation should be a strong inhibitor of the cleavage for two reasons. First, this is because its concentration is higher than that of the active species; for zinc for example, it can be estimated from (56) that $[Zn^{2+}]$ is in 20-fold excess versus $[Zn^{2+}OH^{-}]$. Secondly, the affinity for the anionic binding site of the doubly charged species is certainly also much higher than that of the singly charged species. It is thus tempting to suggest a scenario in two steps. First, such an inactive doubly charged M^{2+} species would indeed bind, and well, but without being protected against the H_2O/OH^{-} exchange. Second, once the cation has been partially neutralized as $M^{2+}(OH^{-})$, and thus transformed *in situ* into the active singly charged species, it would be also more easily released in the immediate vicinity of the cleavable site. Expressed in a metaphoric way, the cleavage would result from some 'Trojan horse' mechanism wherein an apparently 'inoffensive' cation species is hosted next to the cleavage site but, soon or later, is transformed into a more easily released 'aggressive' species. The interesting consequence is that the more tightly bound an inhibitor is, the more chance it has to be transformed *in situ* into the aggressive species. Such an interpretation should be of general extent in situations where a bound cation is active as the general base (as, we think, this holds true in the present case).

Comparison with other cation-dependent ribozyme

This DIS fragment should be viewed as a metal-dependent ribozyme, but certainly not as a very efficient one. There are two reasons for that. First, the necessary conformational change yielding the in-line geometry (Figure 6c) requires a high, and may be even a very high, activation energy. Second, we did not detect any candidate to act as the general acid providing a proton to the leaving group. Very likely, this role is played by a water molecule from the bulk solvent. On the contrary, in very efficient ribozymes, the structure is tuned for a favourable orientation of the cleavable bond and, furthermore, both the general base and the general acid are identified as pre-structured entities. This is the case, for example, for the hepatitis delta virus (HDV) ribozyme where a bound magnesium cation and a cytosine base (C75) were clearly identified. However, somewhat strangely, no definite consensus emerged about which acts as the general acid, and which acts as the general base (46,57–59). A 'multichannel reaction mechanism', instead of a presupposed unique mechanism, could reconcile the opposite views (49). Recently, a new metal ion binding site was described at a position that is consistent with a magnesium-bound hydroxide serving as a general base (60). This would therefore be comparable to our observations.

In the case of the DIS ribozyme, although the role of the cation as the general base seems established, it is unclear whether the hydroxide anion has to be shuttled by the cation to the accepting hydroxyl group, or whether it may simply be released by the cation close to it. In the

first case, the cation would be directly involved into the chemical step (possibly interacting also with the A272 phosphate after its conformational change (Figure 6c), which would stabilize the transition state), whereas in the second case it would act at a distance. In this respect, a thorough comparison with protein enzymes has led to the proposal that a cation can indeed exert a catalytic effect without contacting directly its 'target' (61). This is certainly not against the previous conclusion drawn from the comparison with the artificial system using lanthanide complexes (55).

ACCESSION NUMBERS

Atomic coordinates and structure factors of the native, the manganese- and the cobalt-soaked structures have been deposited with the Protein Data Bank (ID 2OIY, 2OJ0 and 3FAR, respectively).

SUPPLEMENTARY DATA

Supplementary Data are available at NAR Online.

ACKNOWLEDGEMENTS

The authors thank Philippe Carpentier for his abundant support on data collection on the beamline BM30 (ESRF, Grenoble, France), Guillaume Bec for the maintenance of the rotating anode and Philippe Wolff for purification of RNA.

FUNDING

French 'Agence Nationale de Recherche sur le SIDA' (ANRS). Funding for open access charge: Centre National de la Recherche Scientifique (CNRS); Agence Nationale de Recherche sur le SIDA.

Conflict of interest statement. None declared.

REFERENCES

1. St Louis,D.C., Gotte,D., Sanders-Buell,E., Ritchey,D.W., Salminen,M.O., Carr,J.K. and McCutchan,F.E. (1998) Infectious molecular clones with the nonhomologous dimer initiation sequences found in different subtypes of human immunodeficiency virus type 1 can recombine and initiate a spreading infection in vitro. *J. Virol.*, **72**, 3991–3998.
2. Skripkin,E., Paillart,J.C., Marquet,R., Ehresmann,B. and Ehresmann,C. (1994) Identification of the primary site of the Human Immunodeficiency Virus Type I RNA dimerization *in vitro*. *Proc. Natl Acad. Sci, USA*, **91**, 4945–4949.
3. Laughrea,M. and Jetté,L. (1994) A 19-nucleotide sequence upstream of the 5′ major splice donor site is part of the dimerization domain of human immunodeficiency virus 1 genomic RNA. *Biochemistry*, **33**, 13464–13474.
4. Clever,J.L., Wong,M.L. and Parslow,T.G. (1996) Requirements for kissing-loop-mediated dimerization of human immunodeficiency virus RNA. *J. Virol.*, **70**, 5902–5908.
5. Paillart,J.C., Westhof,E., Ehresmann,C., Ehresmann,B. and Marquet,R. (1997) Non-canonical interactions in a kissing loop complex: the dimerization initiation site of HIV-1 genomic RNA. *J. Mol. Biol.*, **270**, 36–49.
6. Paillart,J.-C., Berthoux,L., Ottmann,M., Darlix,J.-L., Marquet,R., Ehresmann,C. and Ehresmann,B. (1996) A dual role of the dimerization initiation site of HIV-1 in genomic RNA packaging and proviral DNA synthesis. *J. Virol.*, **70**, 8348–8354.
7. Berkhout,B. and van Wamel,J.L. (1996) Role of the DIS hairpin in replication of human immunodeficiency virus type 1. *J. Virol.*, **70**, 6723–6732.
8. Clever,J.L. and Parslow,T.G. (1997) Mutant HIV-1 genomes with defects in RNA dimerization or encapsidation. *J. Virol.*, **71**, 3407–3414.
9. Laughrea,M., Jetté,L., Mak,J., Kleinman,L., Liang,C. and Wainberg,M.A. (1997) Mutations in the kissing-loop hairpin of human immunodeficiency virus type 1 reduce viral infectivity as well as genomic RNA packaging and dimerization. *J. Virol.*, **71**, 3397–3406.
10. Laughrea,M. and Jetté,L. (1996) Kissing-loop model of HIV-1 genome dimerization: HIV-1 RNA can assume alternative dimeric forms, and all sequences upstream or downstream of hairpin 248-271 are dispensable for dimer formation. *Biochemistry*, **35**, 1589–1598.
11. Muriaux,D., Fossé,P. and Paoletti,J. (1996) A kissing complex together with a stable dimer is involved in the HIV-1_{Lai} RNA dimerization process *in vitro*. *Biochemistry*, **35**, 5075–5082.
12. Muriaux,D., Rocquigny,H.D., Roques,B.P. and Paoletti,J. (1996) NCP7 activates HIV-1 Lai RNA dimerization by converting a transient loop-loop complex into a stable dimer. *J. Biol. Chem.*, **271**, 33686–33692.
13. Takahashi,K.I., Baba,S., Chattopadhyay,P., Koyanagi,Y., Yamamoto,N., Takaku,H. and Kawai,G. (2000) Structural requirement for the two-step dimerization of human immunodeficiency virus type 1 genome. *RNA*, **6**, 96–102.
14. Takahashi,K.I., Baba,S., Koyanagi,Y., Yamamoto,N., Takaku,H. and Kawai,G. (2001) Two basic regions of NCp7 are sufficient for conformational conversion of HIV-1 dimerization initiation site from kissing-loop dimer to extended-duplex dimer. *J. Biol. Chem.*, **276**, 31274–31278.
15. Bernacchi,S., Ennifar,E., Toth,K., Walter,P., Langowski,J. and Dumas,P. (2005) Mechanism of hairpin-duplex conversion for the HIV-1 dimerization initiation site. *J. Biol. Chem.*, **280**, 40112–40121.
16. Rist,M.J. and Marino,J.P. (2002) Mechanism of nucleocapsid protein catalyzed structural isomerization of the dimerization initiation site of HIV-1. *Biochemistry*, **41**, 14762–14770.
17. Bernacchi,S., Freisz,S., Maechling,C., Spiess,B., Marquet,R., Dumas,P. and Ennifar,E. (2007) Aminoglycoside binding to the HIV-1 RNA dimerization initiation site: thermodynamics and effect on the kissing-loop to duplex conversion. *Nucleic Acids Res.*, **35**, 7128–7139.
18. Fu,W., Gorelick,R.J. and Rein,A. (1994) Characterization of HIV-1 dimeric RNA from wild-type and protease-defective virions. *J. Virol.*, **68**, 5013–5018.
19. Ennifar,E., Yusupov,M., Walter,P., Marquet,R., Ehresmann,B., Ehresmann,C. and Dumas,P. (1999) The crystal structure of the dimerization initiation site of genomic HIV-1 RNA reveals an extended duplex with two adenine bulges. *Structure*, **7**, 1439–1449.
20. Freisz,S., Lang,K., Micura,R., Dumas,P. and Ennifar,E. (2008) Binding of aminoglycoside antibiotics to the duplex form of the HIV-1 genomic RNA dimerization initiation site. *Angew. Chem. Int. Ed. Engl.*, **47**, 4110–4113.
21. Ennifar,E. and Dumas,P. (2006) Polymorphism of bulged-out residues in HIV-1 RNA DIS kissing complex and structure comparison with solution studies. *J. Mol. Biol.*, **356**, 771–782.
22. Ennifar,E., Walter,P., Ehresmann,B., Ehresmann,C. and Dumas,P. (2001) Crystal structures of coaxially stacked kissing complexes of the HIV-1 RNA dimerization initiation site. *Nat. Struct. Biol.*, **8**, 1064–1068.
23. Ennifar,E., Paillart,J.C., Bodlenner,A., Walter,P., Weibel,J.M., Aubertin,A.M., Pale,P., Dumas,P. and Marquet,R. (2006) Targeting the dimerization initiation site of HIV-1 RNA with aminoglycosides: from crystal to cell. *Nucleic Acids Res.*, **34**, 2328–2339.
24. Ennifar,E., Paillart,J.C., Marquet,R., Ehresmann,B., Ehresmann,C., Dumas,P. and Walter,P. (2003) HIV-1 RNA dimerization initiation site is structurally similar to the ribosomal A site and binds aminoglycoside antibiotics. *J. Biol. Chem.*, **278**, 2723–2730.

25. Bodlenner,A., Alix,A., Weibel,J.M., Pale,P., Ennifar,E., Paillart,J.C., Walter,P., Marquet,R. and Dumas,P. (2007) Synthesis of a neamine dimer targeting the dimerization initiation site of HIV-1 RNA. *Org Lett*, **9**, 4415–4418.
26. Ennifar,E., Paillart,J.C., Bernacchi,S., Walter,P., Pale,P., Decout,J.L., Marquet,R. and Dumas,P. (2007) A structure-based approach for targeting the HIV-1 genomic RNA dimerization initiation site. *Biochimie*, **89**, 1195–1203.
27. Ennifar,E., Walter,P. and Dumas,P. (2003) A crystallographic study of the binding of 13 metal ions to two related RNA duplexes. *Nucleic Acids Res.*, **31**, 2671–2682.
28. Otwinowski,Z. and Minor,W. (1996) Processing of X-ray diffraction data collected in oscillation mode. In Carter,C.W. Jr and Sweet,R.M. (eds), *Methods in Enzymology*, Vol. 276A. Academic Press, New York, USA, pp. 307–326.
29. Dumas,P. (1994) The heavy-atom problems: a statistical analysis. I. A priori determination of best scaling, level of substitution, lack of isomorphism and phasing power. *Acta Cryst.*, **A50**, 526–537.
30. Dumas,P. (1994) The heavy-atom problems: a statistical analysis. II. Consequences of the *a priori* knowledge of the noise and heavy-atom powers and use of a correlation function for heavy-atom-site determination. *Acta Cryst.*, **A50**, 537–546.
31. de la Fortelle,E. and Bricogne,G. (1997) Maximum-likelyhood heavy-atom parameter refinement for MIR and MAD methods. In Carter,C.W. Jr and Sweet,R.M. (eds), *Methods in Enzymology*, Vol. 276A. Academic Press, New York, USA, pp. 472–494.
32. Abrahams,J.P. and Leslie,A.G.W. (1996) Methods used in the structure determination of bovine mitochondrial F1 ATPase. *Acta Cryst.*, **D52**, 30–42.
33. Jones,T.A., Zou,J.Y., Cowan,S.W. and Kjeldgaard,M. (1991) Improved methods for the building of protein models in electron density maps and the location of errors in these models. *Acta Cryst.*, **A47**, 110–119.
34. Brunger,A.T., Adams,P.D., Clore,G.M., DeLano,W.L., Gros,P., Grosse-Kunstleve,R.W., Jiang,J.S., Kuszewski,J., Nilges,M., Pannu,N.S. *et al.* (1998) Crystallography & NMR system: A new software suite for macromolecular structure determination. *Acta Cryst.*, **D54**, 905–921.
35. Doherty,E.A., Batey,R.T., Masquida,B. and Doudna,J.A. (2001) A universal mode of helix packing in RNA. *Nat. Struct. Biol.*, **8**, 339–343.
36. Nissen,P., Ippolito,J.A., Ban,N., Moore,P.B. and Steitz,T.A. (2001) RNA tertiary interactions in the large ribosomal subunit: the A-minor motif. *Proc. Natl Acad. Sci. USA*, **98**, 4899–4903.
37. Carter,A.P., Clemons,W.M., Brodersen,D.E., Morgan-Warren,R.J., Wimberly,B.T. and Ramakrishnan,V. (2000) Functional insights from the structure of the 30S ribosomal subunit and its interactions with antibiotics. *Nature*, **407**, 340–348.
38. Paillart,J.C., Marquet,R., Skripkin,E., Ehresmann,B. and Ehresmann,C. (1994) Mutational analysis of the bipartite dimer linkage structure of human immunodeficiency virus type 1 genomic RNA. *J. Biol. Chem.*, **269**, 27486–27493.
39. Laughrea,M. and Jette,L. (1997) HIV-1 genome dimerization: kissing-loop hairpin dictates whether nucleotides downstream of the 5′ splice junction contribute to loose and tight dimerization of human immunodeficiency virus RNA. *Biochemistry*, **36**, 9501–9508.
40. Fedor,M.J. and Williamson,J.R. (2005) The catalytic diversity of RNAs. *Nat. Rev. Mol. Cell Biol.*, **6**, 399–412.
41. Brown,R.S., Dewan,J.C. and Klug,A. (1985) Crystallographic and biochemical investigation of the lead(II)-catalyzed hydrolysis of yeast phenylalanine tRNA. *Biochemistry*, **24**, 4785–4801.
42. Brown,R.S., Hingerty,B.E., Dewan,J.C. and Klug,A. (1983) Pb(II)-catalysed cleavage of the sugar-phosphate backbone of yeast tRNAPhe – implications for lead toxicity and self-splicing RNA. *Nature*, **303**, 543–546.
43. Pan,T. and Uhlenbeck,O.C. (1992) A small metalloribozyme with a two-step mechanism. *Nature*, **358**, 560–563.
44. Lilley,D.M. (2005) Structure, folding and mechanisms of ribozymes. *Curr. Opin. Struct. Biol.*, **15**, 313–323.
45. Takagi,Y., Warashina,M., Stec,W.J., Yoshinari,K. and Taira,K. (2001) Recent advances in the elucidation of the mechanisms of action of ribozymes. *Nucleic Acids Res.*, **29**, 1815–1834.
46. Ke,A., Zhou,K., Ding,F., Cate,J.H. and Doudna,J.A. (2004) A conformational switch controls hepatitis delta virus ribozyme catalysis. *Nature*, **429**, 201–205.
47. Borda,E.J., Markley,J.C. and Sigurdsson,S.T. (2003) Zinc-dependent cleavage in the catalytic core of the hammerhead ribozyme: evidence for a pH-dependent conformational change. *Nucleic Acids Res.*, **31**, 2595–2600.
48. Markley,J.C., Godde,F. and Sigurdsson,S.T. (2001) Identification and characterization of a divalent metal ion-dependent cleavage site in the hammerhead ribozyme. *Biochemistry*, **40**, 13849–13856.
49. Nakano,S., Proctor,D.J. and Bevilacqua,P.C. (2001) Mechanistic characterization of the HDV genomic ribozyme: assessing the catalytic and structural contributions of divalent metal ions within a multichannel reaction mechanism. *Biochemistry*, **40**, 12022–12038.
50. Boots,J.L., Canny,M.D., Azimi,E. and Pardi,A. (2008) Metal ion specificities for folding and cleavage activity in the Schistosoma hammerhead ribozyme. *RNA*, **14**, 2212–2222.
51. Draper,D.E., Grilley,D. and Soto,A.M. (2005) Ions and RNA folding. *Annu. Rev. Biophys. Biomol. Struct.*, **34**, 221–243.
52. Martick,M. and Scott,W.G. (2006) Tertiary contacts distant from the active site prime a ribozyme for catalysis. *Cell*, **126**, 309–320.
53. Wedekind,J.E. and McKay,D.B. (1999) Crystal structure of a lead-dependant ribozyme revealing metal binding sites relevant to catalysis. *Nat. Struct. Biol.*, **6**, 261–268.
54. Zivarts,M., Liu,Y. and Breaker,R.R. (2005) Engineered allosteric ribozymes that respond to specific divalent metal ions. *Nucleic Acids Res.*, **33**, 622–631.
55. Hall,J., Husken,D. and Haner,R. (1996) Towards artificial ribonucleases: the sequence-specific cleavage of RNA in a duplex. *Nucleic Acids Res.*, **24**, 3522–3526.
56. Reichle,R.A., McCurdy,K.G. and Hepler,L.G. (1975) Zinc hydroxyde: solubility product and hydroxy-complex stability constants from 12.5-75°C. *Can. J. Chem.*, **53**, 3841–3845.
57. Nakano,S., Chadalavada,D.M. and Bevilacqua,P.C. (2000) General acid-base catalysis in the mechanism of a hepatitis delta virus ribozyme. *Science*, **287**, 1493–1497.
58. Doudna,J.A. and Lorsch,J.R. (2005) Ribozyme catalysis: not different, just worse. *Nat. Struct. Mol. Biol.*, **12**, 395–402.
59. Lippert,B. (2008) Ligand-pKa shifts through metals: potential relevance to ribozyme chemistry. *Chem. Biodivers.*, **5**, 1455–1474.
60. Chen,J.H., Gong,B., Bevilacqua,P.C., Carey,P.R. and Golden,B.L. (2009) A catalytic metal ion interacts with the cleavage Site G.U wobble in the HDV ribozyme. *Biochemistry*, **48**, 1498–1507.
61. Sigel,R.K. and Pyle,A.M. (2007) Alternative roles for metal ions in enzyme catalysis and the implications for ribozyme chemistry. *Chem. Rev.*, **107**, 97–113.